



JAXA-ONERA-DLR cooperation: results from rotor optimization in hover

Gunther Wilke¹ · Joëlle Bailly² · Keita Kimura³ · Yasutada Tanabe³

Received: 6 October 2021 / Revised: 9 March 2022 / Accepted: 24 March 2022
© The Author(s) 2022

Abstract

A cooperation between JAXA, ONERA and DLR puts the focus on the aerodynamic optimization of helicopter rotors. This paper represents the conclusions from the first phase: optimization of a hovering rotor. The HART-II blade is first investigated with low-fidelity tools and compared against state-of-the-art CFD simulations. Afterwards, the chord distribution and twist of the HART-II blade are optimized using the low-fidelity tools as well as CFD. Since the partners observed differences in the outcome of the CFD simulations for the low-fidelity optimized blades, a deeper investigation of the effects of the turbulence modelling approach, elasticity and grid topology is conducted. The findings show that the chosen flight condition is close to the thrust of the maximum Figure of Merit and that the vortex-triggered separation on the outboard sections of the blade has to be modelled correctly. In this study, the blade grids had the most noticeable effect on the results, followed by the turbulence model and elasticity. With respect to the optimization, low-fidelity methods require special care, whereas CFD optimized blades were found to lead to more robust designs, even though they have only been optimized for a single point. This is explained by the more accurate modelling of the stall phenomenon with respect to geometrical changes.

Keywords Helicopter aerodynamics · Surrogate-based optimization · CFD

1 Introduction

The flow around helicopter rotor blades is of complex nature, due to the vortex-dominated flow and the various speed regimes, which the different blade sections undergo. Thus, the correct simulation of the rotor aerodynamics is a challenging task. Trying to improve current rotor blade designs through numerical optimization to reduce power

requirements is an even more daunting challenge since many simulations are required to arrive at an improved design.

The three research organizations JAXA, ONERA and DLR decided to join forces in June 2019 to tackle these challenges together. The focus lies on the investigation and comparison of the aerodynamic and aero-acoustic optimization and simulation strategies employed by each partner with the goal to improve the optimization processes as well as the obtained designs.

Looking at past endeavours, JAXA has successfully optimized rotor blades for a compound helicopter [1] and worked with DLR in the past on the accurate flow simulation of rotor blades [2]. JAXA and ONERA collaborated in a previous cooperation, optimizing blades in hover and forward flight [3]. ONERA and DLR have an ongoing partnership with a history of successful collaborations, the work on the ERATO rotor being one example [4]. More recently, a joint investigation on the RACER compound helicopter [5] was performed. It was therefore a natural next step to set up a tri-lateral cooperation.

As opposed to a gradient-based optimization using the adjoint method, as used, for example, by Fabiano and Mavripilis [6], Wang et al. [7] or Fitzgibbon [8], this study

✉ Gunther Wilke
gunther.wilke@dlr.de

Joëlle Bailly
joelle.zibi@onera.fr

Keita Kimura
keita.kimura@jaxa.jp

Yasutada Tanabe
tan@chofu.jaxa.jp

¹ German Aerospace Center/DLR, Lilienthalplatz
7, 38108 Braunschweig, Germany

² The French Aerospace Lab/ONERA, 8, rue des
Vertugadins, 92190 Meudon, France

³ Japan Aerospace Exploration Agency/JAXA, Osawa 6-13-1,
Mitaka, Tokyo 181-0015, Japan

analyses a surrogate-based optimization approach [9]. In the first phase of the cooperation, an optimization with five design variables driving the chord and twist distributions of the rotor was carried out, minimizing the required power, i.e., Figure of Merit, of the HART-II rotor [10] in hover. A first paper on that subject, which primarily focused on low fidelity results with initial CFD-based results for the baseline rotor, has been presented [11].

This paper discusses the different outcomes of the low fidelity and high-fidelity optimizations, as well as the effects on different turbulence modelling, grid topologies and the inclusion of elasticity.

2 Methodology

2.1 Low-fidelity setups

The underlying methodology used for the low-fidelity aerodynamics model is the blade-element theory (BET). The sectional forces of the rotor blades are determined from look-up tables of the airfoils. The partners use different inflow models: JAXA utilizes the momentum theory (BEMT), while DLR and ONERA utilize a finite-state model based on the

Table 1 Summary of low-fidelity models

	JAXA	ONERA	DLR
Code	rBET	HOST	
Inflow model	Momentum theory	Finite state	
Radial polynomials		24	8
Structural adjustment	–	Polynomial fit [15]	Linear scaling [16]

Polynomials refer to the number of Legendre polynomials used for the radial representation in the finite state model

work by Peters et al. [12] and implemented into the comprehensive code HOST [13] by Basset et al. [14].

Since both types of inflow models do not feature any tip-vortex modelling, a simple cut-off factor is used as it was found to work better than Prandtl's tip-loss function. The cut-off factor (simply) sets the lift past $r/R=0.95$ to zero, whereas, an angle of attack of zero is used for the look-up of drag and pitching moment. The setups are briefly summarized in Table 1.

2.2 Computational fluid dynamics

All three partners utilize block-structured codes for the simulation of the rotor flows. For brevity, the major features are compared in Table 2. More information is provided in the associated references.

2.3 Grid topology and generation

Since the partners use different meshing tools and CFD codes, it has been difficult to run common setups. However, a minimum quality guideline was agreed upon, as an attempt to ensure sufficiently matching results. The most crucial and also mandatory one was a y^+ spacing of 1 of the first cell, while at least 80 cells were required chord- and spanwise, with roughly 35 cells in the boundary layer.

JAXA generates a baseline grid with Pointwise [34], which is then deformed during optimization to realize the various geometries to be investigated. The entire rotor is embedded into two sets of background grids, an inner grid with a higher point density, and an outer grid, that extends to the farfield boundaries to reduce potential reflections.

ONERA takes a similar approach, but models a single rotor blade within a quarter cylinder using the Chimera technique. A multi-block, deformable mesh of O–H type is generated for the blade mesh, with the root and tip caps modelled in separate grid blocks. The grids of the new rotor designs are generated through a deformation of the baseline

Table 2 CFD solvers and settings

	JAXA	ONERA	DLR
Solver	rFlow3D [17]	<i>elsA</i> [18]	FLOWer [19]
Inviscid scheme	4th order FMCT + SLAU2 [20, 21] With 2nd order finite volume metrics	2nd order JST [22]	4th order FMCT (vA) + SLAU2 [23, 24]
Time integration	Dual time LU-SGS and 4 stage RK [25, 26]	Backward Euler scheme + LU-SGS (steady)	Dual time 5 stage RK + impl. res. smooth. and multigrid [27]
Turb. model	SA-R Fully turbulent [28, 29]	Kok-SST Fully turbulent [30]	SA-R + empirical transition or Menter SST fully turbulent [28, 29, 31, 32]
Rotor motion	Rigid	Elastic, through delta airloads approach [33] with HOST	

grid based on a quaternion approach [35], developed in the in-house QUANTUM code. The background grid is automatically generated using Cassiopee [36], a set of Python modules for pre- and post-processing of CFD computations. The Froude boundary condition is applied to correct the inflow at the farfield through a source/sink model based on the rotor thrust.

DLR uses the in-house grid generator G^3 based on transfinite interpolation like GEROS [37]. Thus, a new grid is automatically generated for each new rotor design. Here, an O–O block is generated with periodic boundaries, which is extended by additional H–O blocks towards the farfield. Such as ONERA, DLR also utilizes the Froude boundary condition on the outer mesh. This mesh is referred to as “monocoque”, since it does not rely on the Chimera/Overset technique. In later supplementary studies, an additional Chimera setup is also prepared with the in-house grid generator and referred to as “chimera”.

Figures 1, 2, 3 show sketches of the individual meshes for the reference rotor. While JAXA works with a Cartesian background grid, ONERA uses a cylindrical background with even spacing, and DLR, which does not use the overset approach, applies varying spacing in the rotor plane, especially in the circumferential direction. In Table 3, a comparison of grid numbers is given. When multiplying the ONERA and DLR grids by four to complete the rotor, the ONERA grid ends up employing the largest number of grid points, while JAXA and DLR have comparable numbers of grid points.

2.4 Optimization framework

The general optimization approach for this work is based on the EGO optimization algorithm by Jones et al. [38]. A Kriging surrogate model is built after an initial data sampling, and the next infill point is sought using the maximum expected improvement. However, variations in the implemented frameworks exist and are listed in Table 4.

The low-fidelity optimizations are carried out solely with the standard Kriging model. For the high-fidelity optimizations, ONERA and DLR make use of the variable-fidelity approach, which enhances the Kriging model with high-fidelity data. ONERA utilizes the low-fidelity model based on the finite-state inflow for Kriging, combined with high fidelity data obtained from CFD/CSD coupling for Co-Kriging. DLR generates CFD data using a factor eight coarsened grid and Hierarchical Kriging.

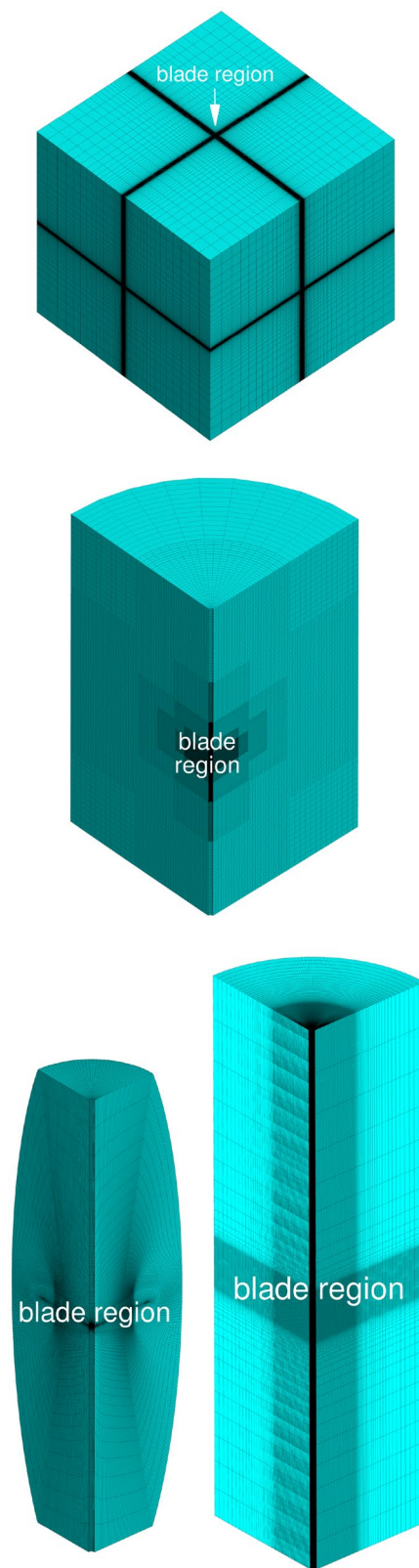


Fig. 1 Isometric views of employed grids. Top: JAXA, center ONERA, bottom left DLR monocoque, bottom right DLR chimera

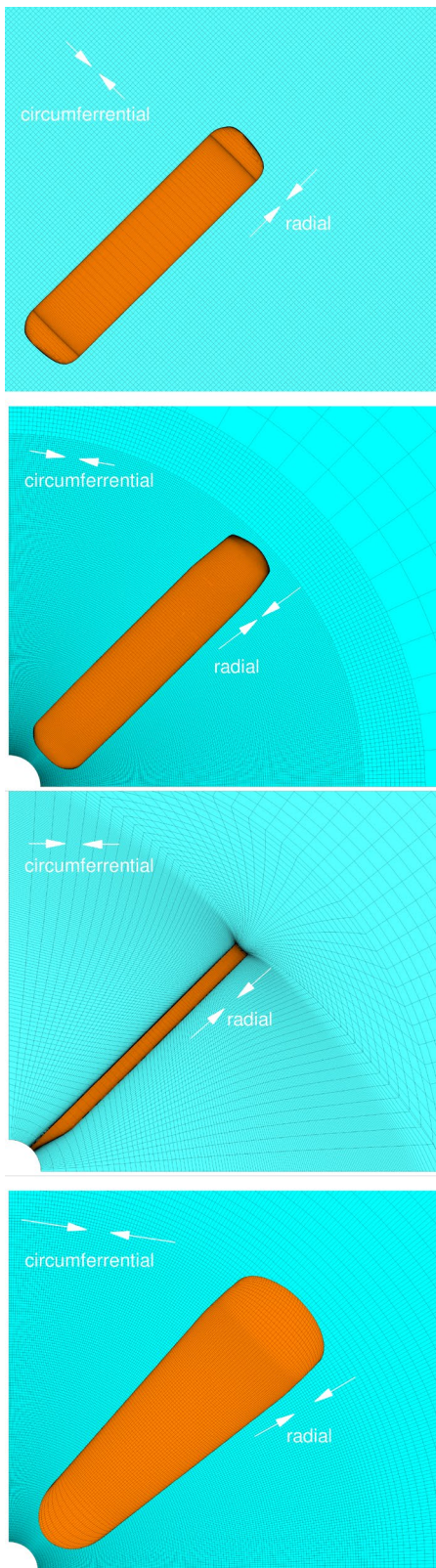


Fig. 2 Top view of blade (orange) and background mesh (cyan). Top: JAXA, center: ONERA, bottom: DLR monocoque and chimera

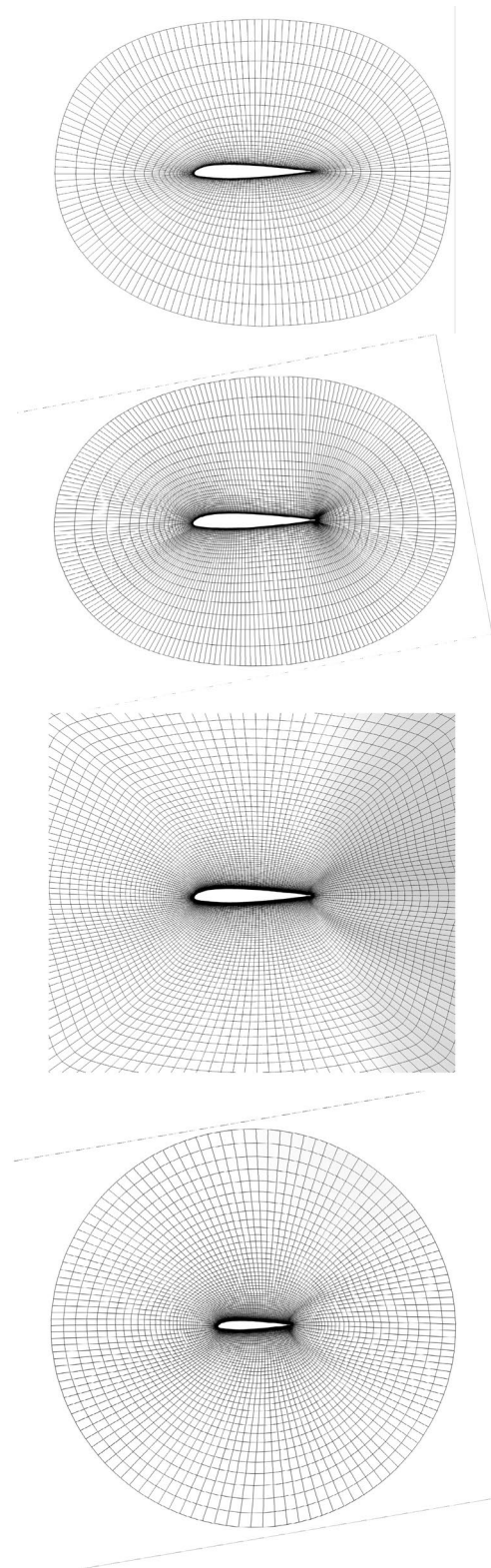


Fig. 3 Cut through the blade mesh at $r/R=0.9$. Top: JAXA, center: ONERA, bottom: DLR monocoque and Chimera

Table 3 Grid properties of each partner's mesh

	JAXA	ONERA	DLR Mono	DLR Chim
Blade mesh cells				
Chordwise	160	80	160	129
Spanwise	120	80	160	129
Boundary layer	~ 50	~ 35	~ 35–60	~ 35–50
Wake resolution (in % chord length)				
Circum-ferential	20	7	9–100	13
Radial			9	13
Vertical			13	14
Farfield/outer grids dimensions (in rotor radii)				
Vertical	100	6	6	6
Lateral	100	6	2.5	2.8
Total # of cells	16 M	6.7 M	4.4 M	7.6 M
Full rotor equivalent	16 M	26.8 M	17.6 M	30.4 M

Table 4 Optimization frameworks

	JAXA	ONERA	DLR
Frame-work	[39, [40]	KORRIGAN [41]	POT [9]
Meta model	Kriging	Co-Kriging [42]	Hierarchical Kriging [43]
Opti-mizer	Genetic algorithm [44, 45]	Diff. Evolution + Nelder and Mead	[46, 47]

Table 5 HART-II rotor specifications and investigated flight condition

Parameter	Value
Number of blades	4
Radius	2 m
Chord	0.121 m
Twist	$- 8^\circ/R$
Airfoil	NACA23012 with tab
Shape	rectangular
Ambient pressure	290.46° K
Ambient temperature	100,970 Pa
RPM	1042
Set thrust	5582 N

3 Optimization task

For this study, the HART-II rotor is selected as the reference rotor, as it is well documented with openly available data [10] and features a simple geometry. The baseline test environment is copied, yet the rotor is placed in a

Table 6 Design variables

Variable	Location	Limits
$\Delta\theta_1$	87.5% r/R	$\pm 5^\circ$
$\Delta\theta_2$	100% r/R	$- 10^\circ-0^\circ$
r_c	–	65–85% r/R
Chord ₁	$r=r_c$	1.0–1.5 c_{ref}
Chord ₂	100% r/R	0.5–1.0 c_{ref}

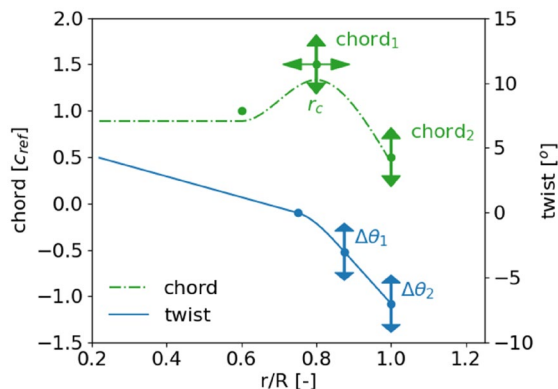


Fig. 4 Sketch of design variables. The chord line does not match the chord parameters as it is scaled to match the same thrust weighted solidity as the HART-II rotor

hover condition with a blade loading of $c_T/\sigma=0.1$, which is trimmed by the collective pitch. The flight condition is summarized in Table 5.

The objective (function) of this study is the maximization of the Figure of Merit defined as

$$FM = \frac{c_T^{1.5}}{\sqrt{2}c_Q}$$

With c_T and c_Q being the thrust and torque coefficients of the rotor. Since the rotor is trimmed to a set thrust, this is the same as minimizing the required power.

A total of five design parameters is utilized: two chord lengths, the radial position of the inner length and two twist parameters. The focus is laid upon modifying the blade tip, where the dynamic pressure is highest. The parameterization description is achieved through cubic splines. The chord distribution is set up with respect to the reference chord length c_{ref} of 0.121 m and is scaled afterwards to match the thrust weighted solidity of the HART-II rotor. Thus, all optimized rotors operate at the same thrust as well as blade loading. The twist spline is applied in Δ -form, meaning that it is added to the existing linear twist with a gradient of $- 8^\circ/R$. The design variables and their limits are listed in Table 6, with a sketch given in Fig. 4. To keep the study sufficiently simple and to not introduce any more severe aeroelastic

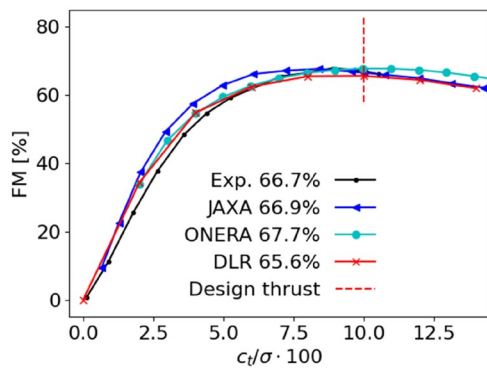


Fig. 5 Figure of Merit polar of HART-II rotor for the low-fidelity methods. Experimental data from [48]

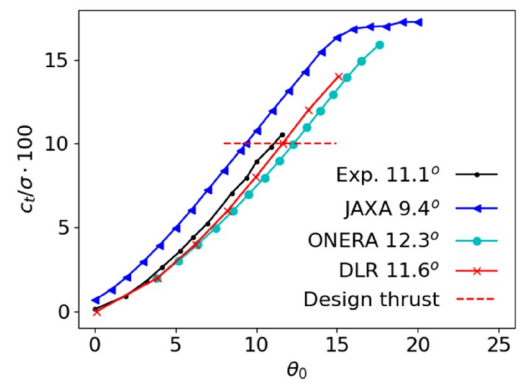


Fig. 7 Blade loading over collective pitch angle for the low-fidelity methods of the HART-II rotor

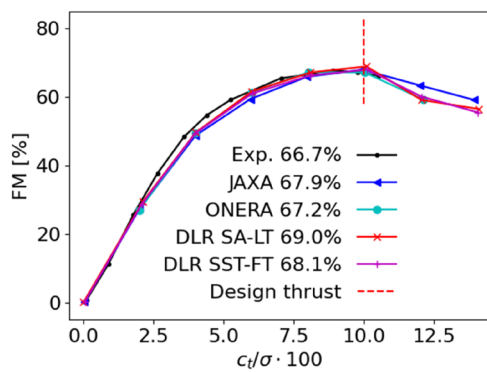


Fig. 6 Figure of Merit polar of HART-II rotor for the CFD simulations. Experimental data from [48]

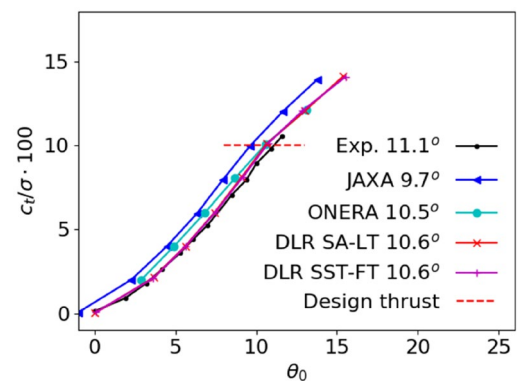


Fig. 8 Blade loading over collective pitch angle for the CFD simulations of the HART-II rotor

effects from blade sweep or an-/dihedral, no further design variables are chosen.

4 Baseline results

As a first measure, the results for the chosen baseline rotor are presented, which happen to summarize the previous paper [11]. In Figs. 5 and 6, the Figure of Merit polars of the low-fidelity and CFD simulations are plotted, respectively. The DLR CFD simulations are split into SA-LT and SST-FT, referencing the application of the Spalart–Allmaras (SA) turbulence model with laminar-turbulent (LT) transition predictions, and the Menter SST model in fully turbulent (FT) mode. While the rough estimate for the Figure of Merit at design thrust can be replicated with the low-fidelity models, the functional behaviour is more accurately replicated by the CFD simulations with respect to the experimental data [48]. Also, variations among the partners' results are less significant for the CFD simulations.

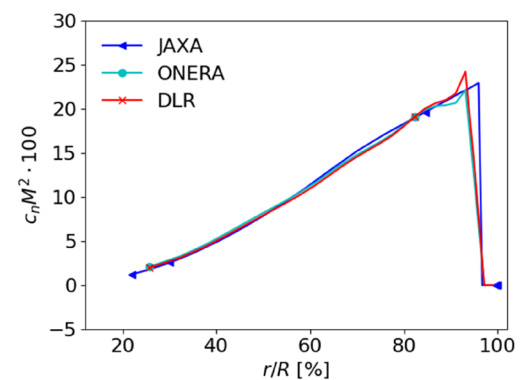


Fig. 9 Normal load distribution of HART-II rotor for low-fidelity methods at design thrust

This is additionally noticeable in Figs. 7 and 8, which display the blade loading over collective pitch for the low-fidelity and CFD simulations, respectively. The variations in results from the partners are lower for the CFD simulations compared to the low-fidelity simulations. The CFD results

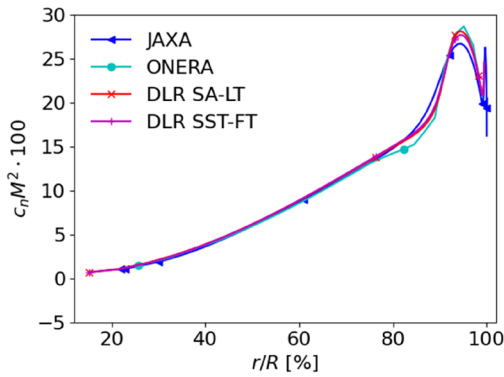


Fig. 10 Normal load distribution of HART-II rotor for CFD simulations at design thrust

are also closer to the experimental values, except for DLR. Their error remains of similar magnitude.

Presenting more details, the normal load distributions at the design thrust are found in Figs. 9 and 10. By comparing the low-fidelity results with the CFD data, it is seen that the behaviour towards the blade tip past $r/R > 80\%$ of the two general approaches is significantly different. The low-fidelity methods capture a mostly linear trend and then drop off at the cut-off value due to the tip loss factor. For the CFD-based methods, the added lift from the upwash from the blade tip vortex of the previous blade shows an increase in the lift gradient, which then drops off at the tip due to the current blade’s tip vortex. Among the individual loads obtained by the partners, minor differences are noticed, which are deemed acceptable, given the stated applied mesh resolution.

The pressure distribution for a radial cut at $r/R = 95\%$ is plotted in Fig. 11 for the design thrust condition. Only minor differences are observed concerning the suction peak. The suction peak of the ONERA results is the closest to the leading edge, whereas JAXA’s suction peak is

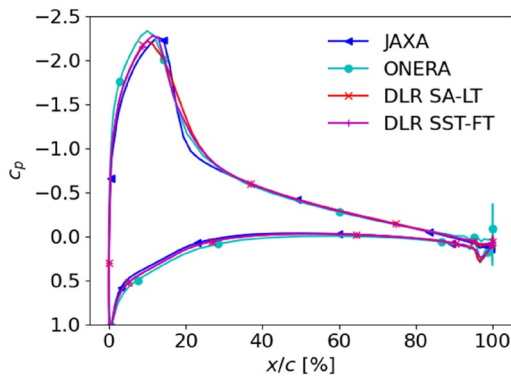


Fig. 11 Pressure distribution of the HART-II rotor @ $r/R=95\%$ and design thrust

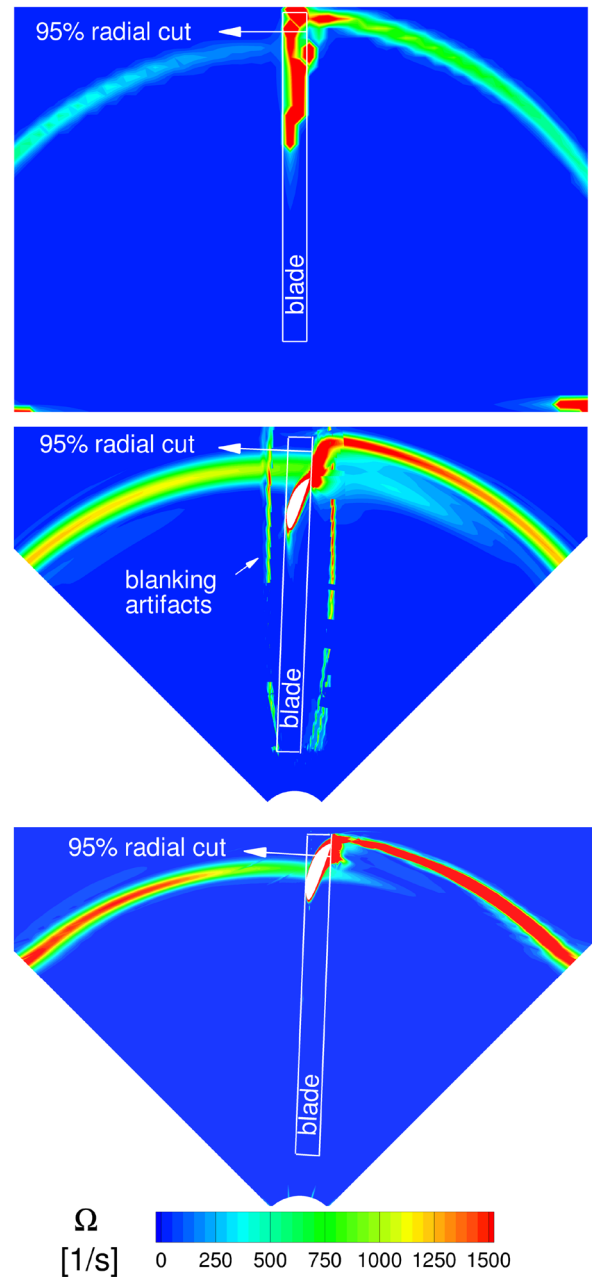


Fig. 12 Vorticity plots of HART-II CFD simulations by the individual partners. Cut through the thrust axis 0.1 m above the rotor center. Top: JAXA, middle: ONERA, bottom DLR. Remade from [11]

the furthest away and the DLR results are in between. The reason for selecting this cut is its location in the upwash area of the previous tip vortex. A stronger tip vortex causes suction peaks that are higher and closer to the leading edge. This also leads to a higher peak in the normal load distribution. Refer to Fig. 12 for a comparison of the vortex conservation of the individual grids. JAXA loses most of the tip vortex strength at the interpolation boundary, whereas a gradual decline is observed with the ONERA

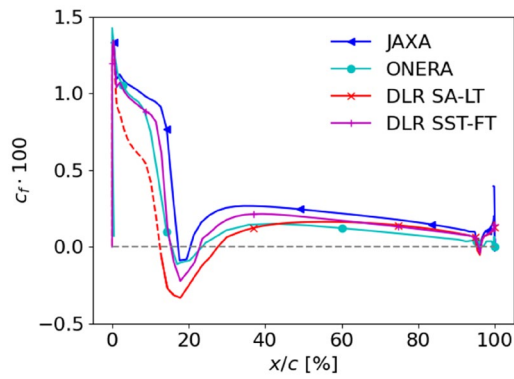


Fig. 13 Suction side skin friction distribution of the HART-II rotor @ $r/R=95\%$ and design thrust. Dashed lines mark laminar regions

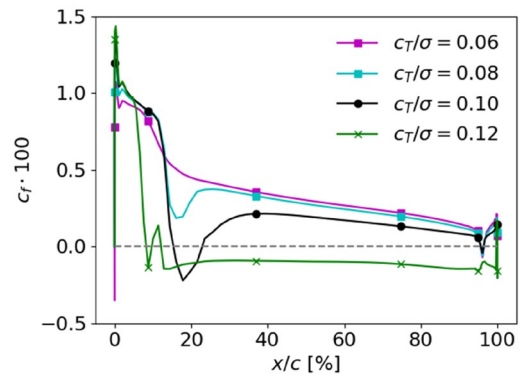


Fig. 15 Suction side skin friction distribution of the HART-II rotor @ $r/R=95\%$ and various thrusts for DLR SST-FT simulations

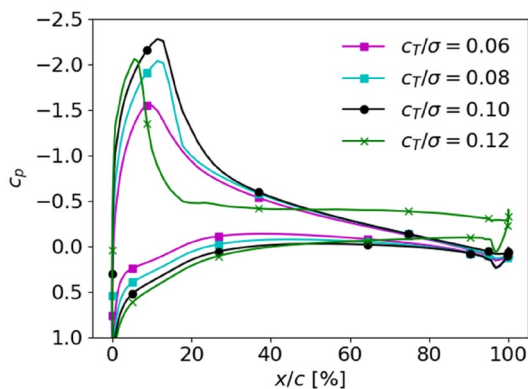


Fig. 14 Pressure distributions of the HART-II rotor @ $r/R=95\%$ and various thrusts for DLR SST-FT simulations

findings. Even though the vortex conservation for DLR remains high for most of the revolution, the strength of the oncoming tip vortex at the blade is of similar magnitude when compared to the ONERA result.

Figure 13 shows the skin friction distributions retrieved for the cut at $r/R=95\%$ for each partner's CFD result. JAXA's skin friction is overall higher than the skin friction evaluated by ONERA and DLR. For all partners, the skin friction dips across a small area just before $x/c \approx 20\%$. This is most dominantly pronounced for DLR's laminar turbulent simulation, followed by DLR's fully turbulent simulation, ONERA and JAXA present similarly pronounced results.

In combination with the pressure distribution, the skin friction plots help to identify separated areas. This is exemplary shown in the pressure distribution in Fig. 14 and the skin friction distribution in Fig. 15. The here plotted distributions are simulated with the DLR SST-FT model for varying blade loadings. With increasing

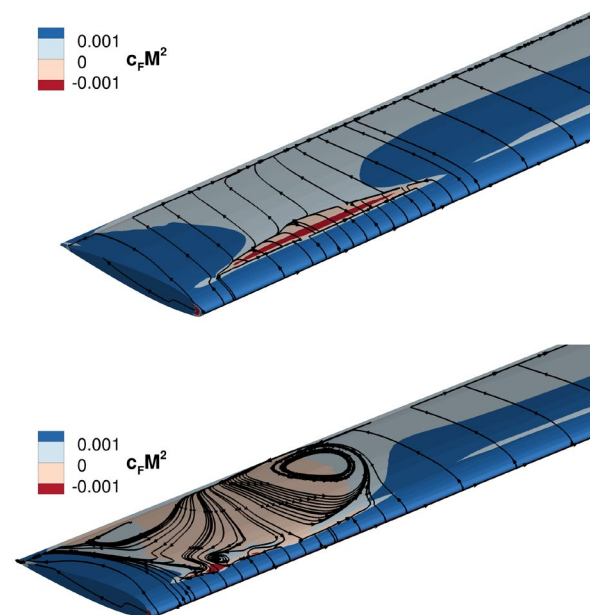


Fig. 16 Skin friction contours for the HART-II rotor. Top: $c_T/\sigma=0.10$, bottom $c_T/\sigma=0.12$. Blue: forward flow, red: reversed flow

thrust, the suction peak grows until it collapses with the highest thrust at $c_T/\sigma=0.12$. The dip in skin friction builds up with increasing thrust to the point of the highest thrust level, after which the skin friction remains negative. Looking at the binary skin friction contour plots in Fig. 16, it is observed that for $c_T/\sigma=0.10$, only a small separation bubble is noticeable, while for the higher thrust at $c_T/\sigma=0.12$, a severe separation is visible, which is caused by the oncoming tip vortex in combination with the increased blade pitch.

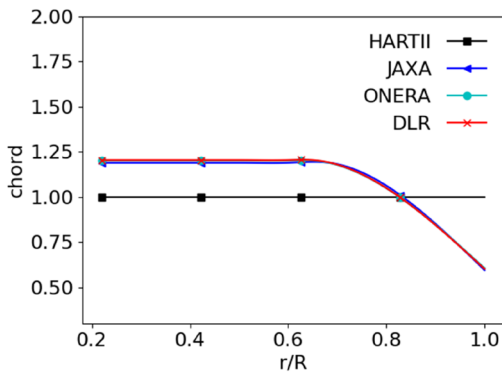


Fig. 17 Chord distribution of low-fidelity optimized blades

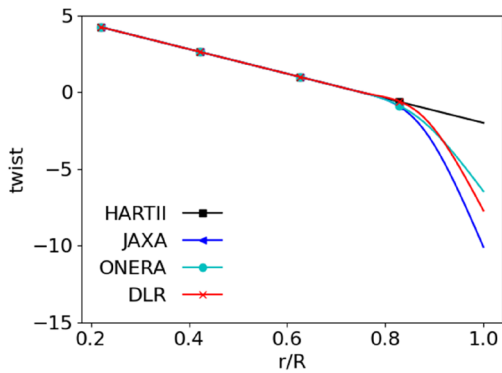


Fig. 18 Twist distribution of low-fidelity optimized blades

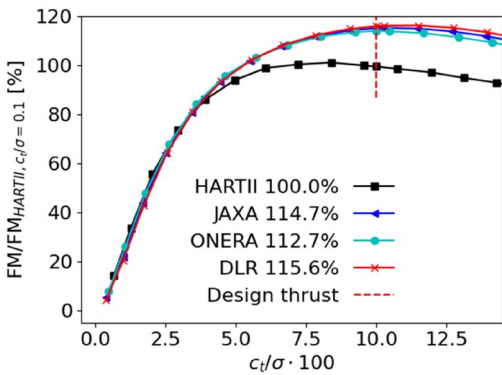


Fig. 19 Figure of Merit polars for low-fidelity optimized blades computed by JAXA's low-fidelity approach

5 Low-fidelity optimized BLADES

The distribution of parameters of the low-fidelity optimized blades is plotted in Fig. 17 for the chord and in Fig. 18 for the twist parameters. It shows very high agreement among the chord parameters, while there are visible

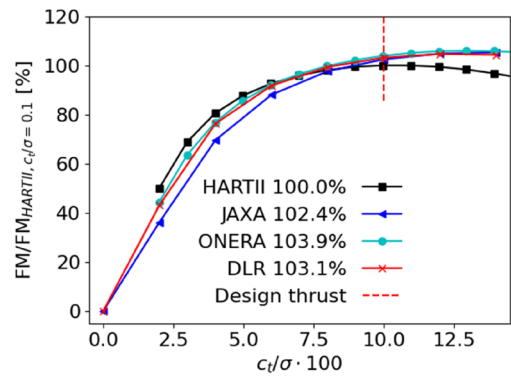


Fig. 20 Figure of Merit polars for low-fidelity optimized blades computed by ONERA's low-fidelity approach

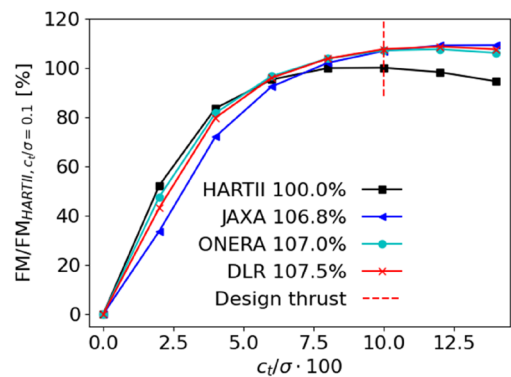


Fig. 21 Figure of Merit polars for low-fidelity optimized blades computed by DLR's low-fidelity approach

differences between the twist parameter, especially at the tip. JAXA features the steepest twist gradient with an offset of $\Delta\theta_2 = -8.1^\circ$, whereas the ONERA blade has a $\Delta\theta_2 = -3.3^\circ$ and the DLR blade is in between with $\Delta\theta_2 = -5.7^\circ$. Even though DLR and ONERA apply the same comprehensive code, it is found that the different number of radial harmonics employed in the finite state model (Table 2) has a noticeable impact on the solution, which explains the differences between the DLR and ONERA blades.

With respect to the Figure of Merit of the blades, all values reported by each partner improve noticeably compared to the reference blade when computed with the low-fidelity methods, refer to Figs. 19, 20 and 21. The results are scaled with the respective Figure of Merit of the HART-II blade at design thrust to see how the relative improvement is captured among the partners. It is not surprising that the individual blades by each partner show the best results when evaluated with the methods they have been optimized with, with the exception of JAXA, which shows a slightly better assessment of the DLR blade. JAXA reports the largest gain

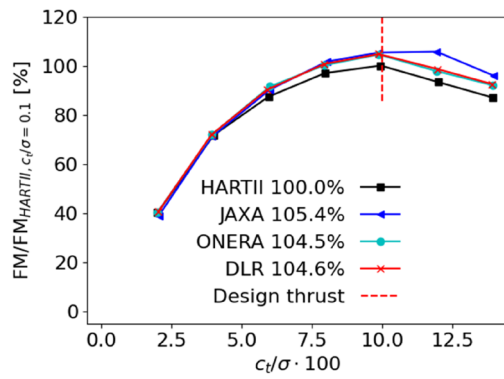


Fig. 22 Figure of Merit polars for low-fidelity optimized blades computed by JAXA's CFD approach

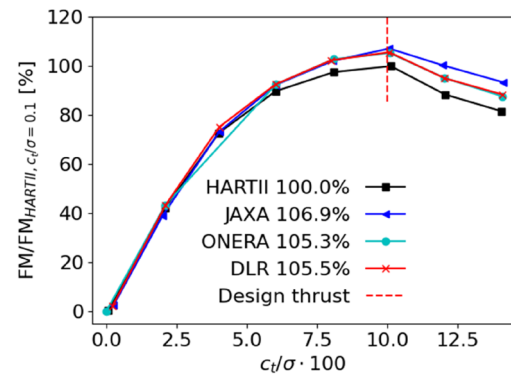


Fig. 25 Figure of Merit polars of low-fidelity optimized blades computed by DLR's CFD approach (SST FT)

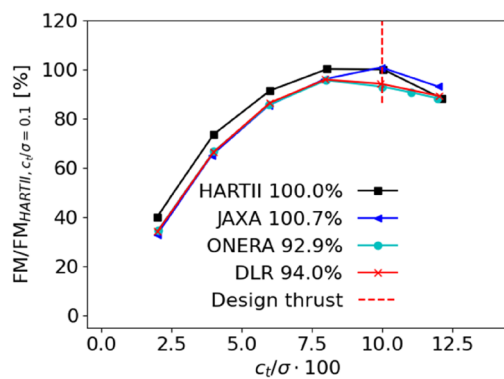


Fig. 23 Figure of Merit polars for low-fidelity optimized blades computed by ONERA's CFD approach

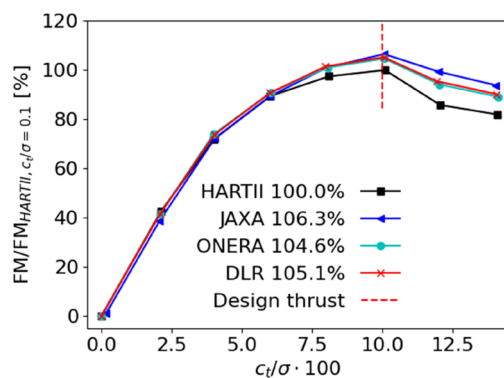


Fig. 24 Figure of Merit polars for low-fidelity optimized blades computed by DLR's CFD approach (SA-R LT)

concerning the Figure of Merit of the new blades, whereas ONERA the smallest.

A cross-examination of all these blades is undertaken by each partner with their CFD methods to assess the gains achieved by the low-fidelity optimizations and to see how

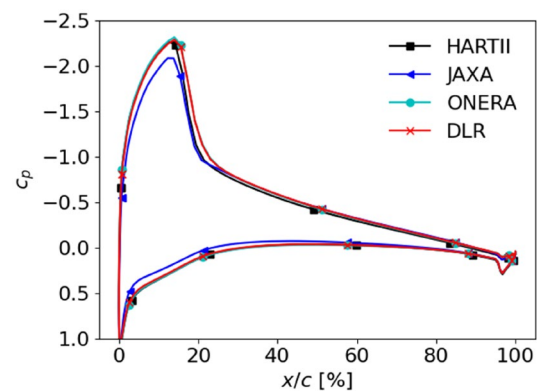


Fig. 26 Pressure distribution of the low-fidelity optimized blades @ $r/R = 95\%$ and design thrust for JAXA's CFD simulations

far the gap is among the partners for resolving individual rotor geometries.

The Figure of Merit polars computed by JAXA are shown in Fig. 22, by ONERA in Fig. 23 and by DLR in Figs. 24 and 25. The actual values are scaled with the Figure of Merit of the HART-II reference blade at design thrust as reported by each partner's CFD code to better visualise the gains of each blade. It is noteworthy that all JAXA and DLR low-fidelity optimized blades improve over the HART-II blade. The predictions with a laminar-turbulent transition by DLR show greater gains than those using DLR's fully turbulent simulations. These results are closer to JAXA's fully turbulent results, even though the gains are slightly higher for DLR in general. Also, the ranking of blades is similar to JAXA, with JAXA's blade performing best due to the high outboard twist, followed by DLR's and ONERA's blade in descending order of the (negative) outboard twist. In contrast, the ONERA results only show a moderate improvement for the JAXA blade, while the DLR blade performs worse and the ONERA blade performs even lower compared to the baseline blade. When excluding the HART-II blade, the ranking

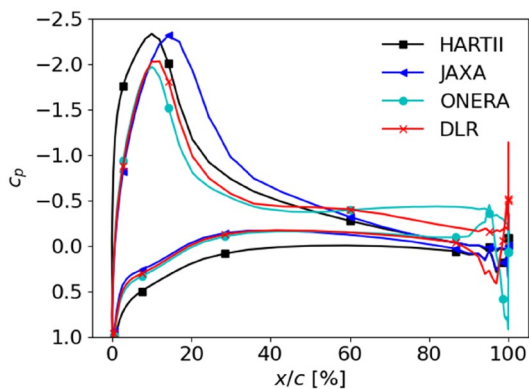


Fig. 27 Pressure distribution of the low-fidelity optimized blades @ $r/R=95\%$ and design thrust for ONERA's CFD simulations

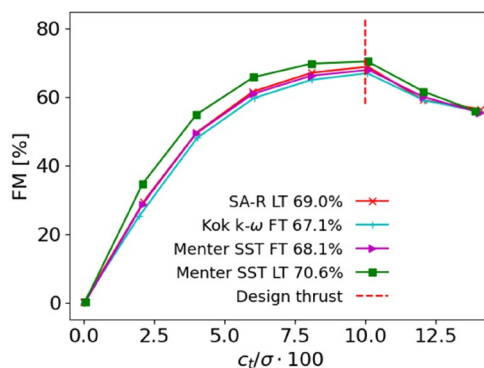


Fig. 30 Figure of Merit polars of the HART-II for different turbulence modelling strategies using DLR's CFD approach

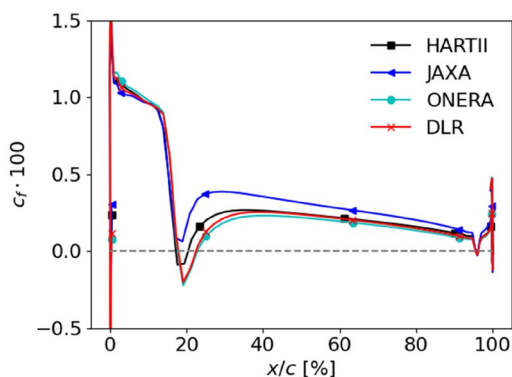


Fig. 28 Suction side skin friction distribution of low-fidelity optimized blades @ $r/R=95\%$ and design thrust for JAXA's CFD simulations

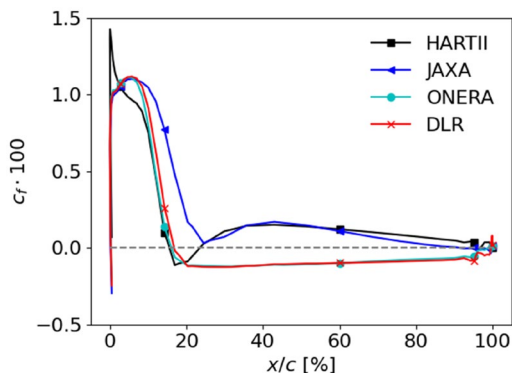


Fig. 29 Suction side skin friction distribution of low-fidelity optimized blades @ $r/R=95\%$ and design thrust for ONERA's CFD simulations

among the blades remains the same. Nevertheless, this is an unexpected outcome.

With JAXA's and ONERA's results showing the greatest differences, the pressure distributions as well as the skin friction distributions are compared against each other in Figs. 26, 27, 28 and 29. JAXA's results offer up a more pronounced dip of the skin friction for the ONERA and DLR blades than for the HART-II blade, and a lesser dip for the JAXA blade, while the pressure distribution remains fairly similar for all blades, with the exception of the JAXA blade, whose peak is reduced. No signs of separation are found. Looking at ONERA's pressure distribution, a rise in pressure drag is identified for the optimized blades, especially the ONERA blade shows signs of a strong separation followed by the DLR blade. This is additionally confirmed by the skin friction plot of the ONERA results, which show evidence of reverse flow past $x/c = 20\%$ until the trailing edge. For the JAXA blade, no signs of separation are observed, but a higher skin friction than the reference blade of up to $x/c = 25\%$ is visible, explaining ONERA's results finding only little gain for this blade over the reference blade.

6 Impact of numerical modelling parameters

Due to the contradicting results in the cross-examination of the low-fidelity blades, it has been decided to systematically look at the effect of turbulence models, the effect of elasticity, and grid topologies on the here presented results. The focus is especially put on the ONERA optimized blade and its performance in contrast to the HART-II rotor. The ONERA blade has been chosen due to performing worst in ONERA's CFD simulations, and also showing the least improvement among the other low-fidelity blades, when cross-examined by the other partners.

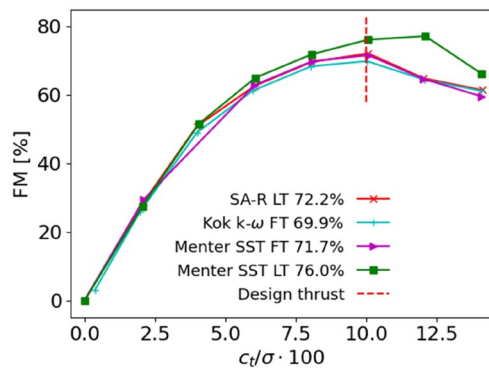


Fig. 31 Figure of Merit polars of the low-fidelity optimized blade by ONERA for different turbulence modelling strategies using DLR's CFD approach

6.1 Effect of turbulence models

Comparative studies of various turbulence models are carried out by DLR and ONERA. Besides the already shown SA-R LT results with laminar-turbulent transition predictions and fully turbulent Menter SST results, additional simulations are executed with the Kok $k-\omega$ turbulence model, as well as laminar-turbulent transition prediction results with the Menter SST model using the given DLR grid setup.

Figure 30 shows the results computed by DLR for the reference blade, while Fig. 31 shows the DLR results for ONERA's low-fidelity optimized blade. For both rotors, the Kok $k-\omega$ turbulence model delivers the lowest curves, while the Menter-SST model with laminar-turbulent transition predicts the highest curves. The range of the Figure of Merit at design thrust is 3.5% for the HART-II rotor, and 6.4% for the ONERA blade, which is considered a noteworthy gap. Yet, looking at the fully turbulent results of the two

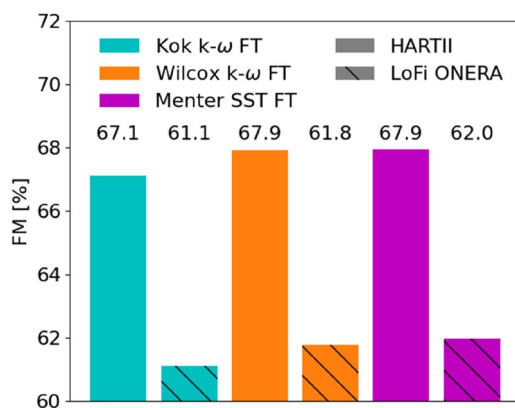


Fig. 32 Figure of Merits @ design thrust with different turbulence models for the ONERA CFD setup

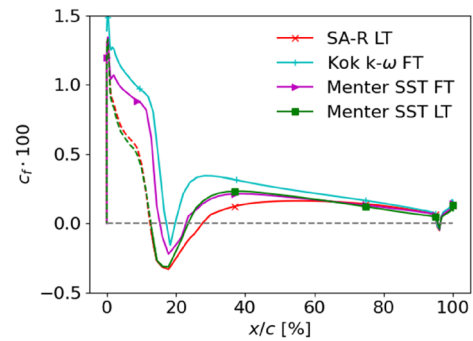


Fig. 33 Suction side skin friction distribution @ $r/R=95\%$ and design thrust for the HART-II rotor using various turbulent modelling strategies using DLR's CFD approach. Dashed lines mark laminar regions

equations models (Kok $k-\omega$ FT and Menter SST FT), these gaps reduce to 1.0% and 1.8%.

ONERA also carried out a study of varying turbulence models for the two rotors. Their reported Figure of Merit at design thrust is visualized in Fig. 32. A similar tendency as for DLR is observed, i.e., the Kok $k-\omega$ model yields overall smaller Figures of Merit, whereas the Menter SST delivers higher Figures of Merit, making it a consistent observation. However, in contrast to the DLR results, the low-fidelity optimized blade deteriorates noticeable with all turbulence models employed by ONERA compared to the reference blade. The difference between the models is 0.8% and 0.9%.

Since the turbulence model mostly influences the viscous effects, the skin friction distribution of the HART-II rotor is plotted in Fig. 33. For the DLR results, the onsets of separation caused by the high upwash velocities, which are induced by the tip vortex of the preceding blade, are seen. They are most pronounced for the SA-R LT setting and for the Menter SST LT setting. Opposing this, the Kok $k-\omega$ model predicts the most overall skin friction and thus delivers the smallest Figure of Merit at design thrust. Despite these results, the strong deterioration, as observed by ONERA, of the ONERA optimized low-fidelity blade cannot be purely explained by the effect of the turbulence models, and only a small impact can be attributed to using the Kok $k-\omega$ model over different turbulence models. The laminar-turbulent transition prediction has a greater impact on the results than the underlying turbulence model.

6.2 Elasticity

A rather brief section is dedicated to the different elastic modeling approaches. Imiela [49, 50] shows in his work the importance of incorporating fluid-structure coupling in the rotor blade optimization for rotors of similar size as used in this study. Stanger et al. [51] demonstrate that the way of obtaining new structural-dynamic properties for a new

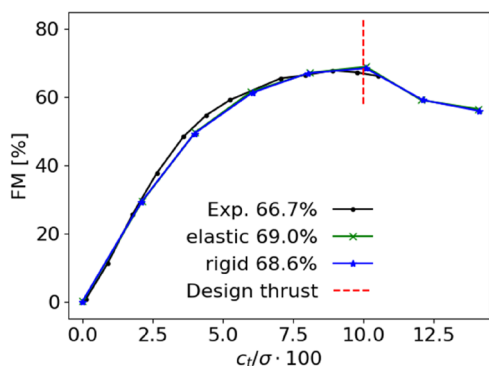


Fig. 34 Figure of Merit polars for rigidly and elastically modelled HART-II blade computed by DLR’s CFD approach (SA-R LT)

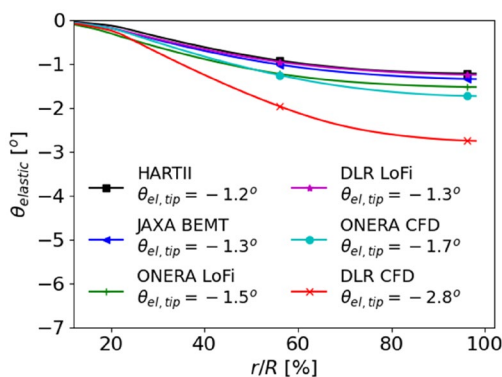


Fig. 35 Torsional deformation for investigated blades using DLR’s CFD simulation (SA-R LT)

aerodynamic shape can have a noticeable effect on the performance, while Desvigne et al. [52] probably have the most advanced approach to update the structural layout of the blade with respect to geometric changes aimed at improving the aerodynamics of a rotor blade.

For the HART-II blade, the effect of neglecting elasticity in this flight condition is small, as can be inferred from the Figure of Merit polar in Fig. 34. The variation is below the effect of varying the turbulence model. The reason for the elastic blade showing a better Figure of Merit at design thrust lies in the structural torsion at the tip, which is about 1.2° for the DLR simulations and 0.6° for the ONERA simulations.

For a look at the other designs investigated in this paper, the torsional deformation and the final blade pitch are plotted in Fig. 35. Most blades feature a fairly similar deformation to the HART-II blade, except DLR’s CFD optimized blade, which is introduced in Sect. 7. For the similarly deformed blades, it may be assumed that the effect mostly leads to a shift of the rigid and elastic simulations of the FM polar, analogously to the HART-II blade.

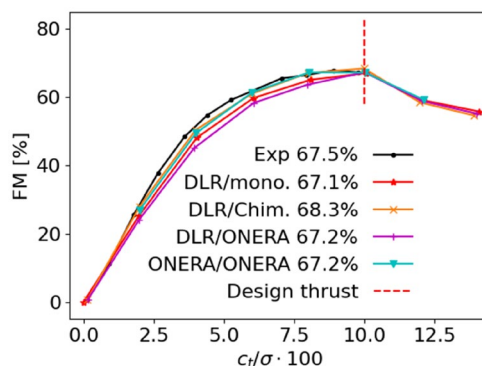


Fig. 36 Figure of Merit polars for the HART-II rotor using different solvers and grids (DLR/mono.=DLR solver and DLR mono-coque grid, DLR/Chim=DLR solver and Chimera setup, DLR/ONERA=DLR solver and ONERA grid, ONERA/ONERA=ONERA solver and grid). Kok $k-\omega$ turbulence model

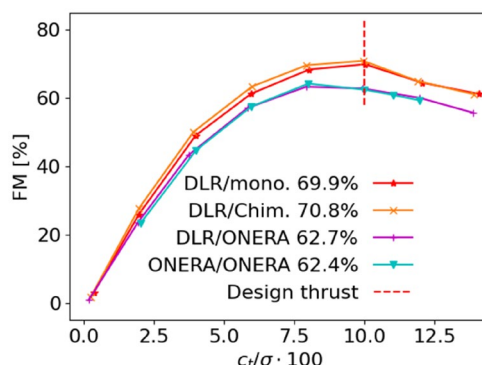


Fig. 37 Figure of Merit polars for the low-fidelity optimized ONERA blade using different solvers and grids (DLR/DLR=DLR solver and DLR grid, ONERA/ONERA=ONERA solver and grid). Kok $k-\omega$ turbulence model

6.3 Grid topologies

Since the effect of the turbulence and elastic modelling alone cannot explain the contradiction of the CFD results concerning the low-fidelity blade optimized by ONERA, the effect of the grid is investigated. Thus, DLR simulated the ONERA blade grids for the HART-II and the low-fidelity optimized grid and resembled ONERA’s CFD settings as close as possible, namely using 2nd order JST scheme and Kok $k-\omega$ turbulence model in fully turbulent mode. The other DLR setup, as mentioned in Sect. 2.2, is now also investigated. The two setups are referred to as DLR/monocoque and DLR/Chimera.

The comparison for the HART-II blade is displayed in Fig. 36 and for the low-fidelity optimized ONERA blade in Fig. 37. While the results align well for the HART-II rotor with minor variations, the results for the optimized blade clearly show the culprit for the discrepancies observed

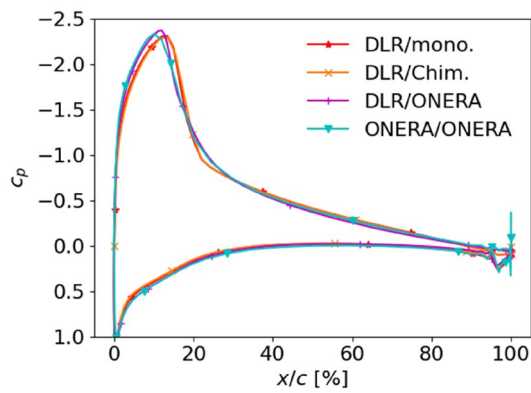


Fig. 38 Pressure distribution @ $r/R=95\%$ and design thrust for the HART-II rotor using different solvers and grids

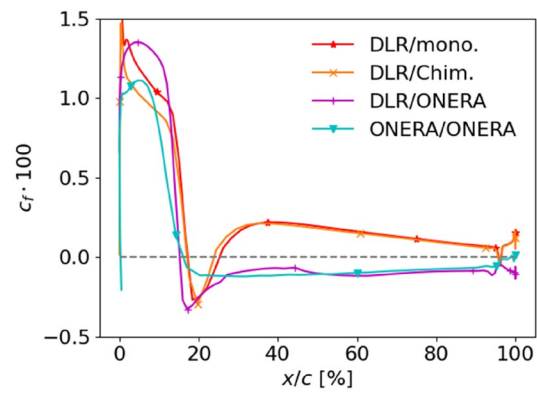


Fig. 41 Suction side skin friction distribution @ $r/R=95\%$ and design thrust for the ONERA low-fidelity optimized rotor using different solvers and grids

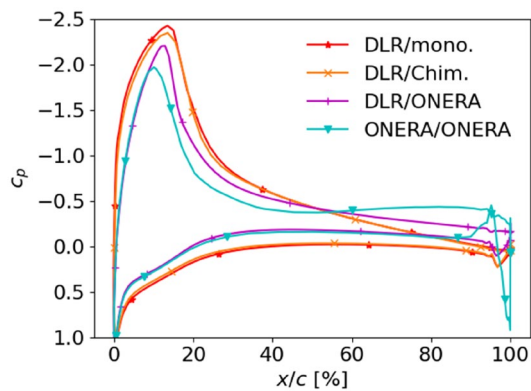


Fig. 39 Pressure distribution @ $r/R=95\%$ and design thrust for the ONERA low-fidelity optimized rotor using different solvers and grids

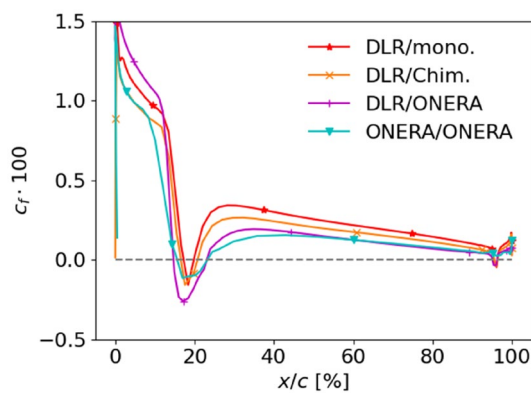


Fig. 40 suction side skin friction distribution @ $r/R=95\%$ and design thrust for the HARTII rotor using different solvers and grids

earlier. The ONERA and DLR solvers report a similar deterioration of the optimized blade when using the ONERA grid and settings, whereas the DLR monocoque and Chimera grids show a favorable behavior for this blade.

DLR repeated the exercise using the SA-R turbulence model without transition prediction on the ONERA grid, applying the 4th order upwind scheme, to find a drop in Figure of Merit from 70.0% for the HART-II blade to 61.0% for the low-fidelity optimized ONERA blade, additionally underlining the grid effect. Duplicating the same with the DLR chimera setup, yields numbers of 68.5% and 67.5% for the HART-II and ONERA low-fidelity optimized blade, respectively.

Further investigating this matter, the pressure and skin friction distributions of the HART-II and ONERA low-fidelity optimized blade are plotted in Figs. 38, 39, 40 and 41. The pressure distributions of the HART-II blade appear very similar, just as it has been the case for the Figure of Merit polars. For the skin friction distribution, greater discrepancies are observed. The result by DLR reflecting the ONERA mesh shows the lowest dip after initially finding the highest peak. Moving on to the ONERA low-fidelity optimized blade, greater offsets are identified. While the DLR monocoque and Chimera setups yield similar results, the DLR result on the ONERA mesh deviates from the ONERA result on its mesh. The pressure distribution results by DLR show only a little rise in pressure drag, whereas the ONERA results of the pressure distribution indicate a strong separation. Moving on to the skin friction, the DLR meshes show a small negative dip of the skin friction, just as they did for the HARTII rotor, while both DLR and ONERA predict reverse flow when using the ONERA mesh. The ONERA and DLR results differ insofar as to the dipping effect is visible with DLR, whereas ONERA does not resolve this. Circling back to the Figure of Merit plot of this blade, this can explain the small deviation at design thrust, and the effects cancel each other out. While DLR and ONERA results differ using the same mesh, the fact that both simulations predict a separation is evident, and minor implementation differences likely lead to more drastic changes in the vicinity of stall.

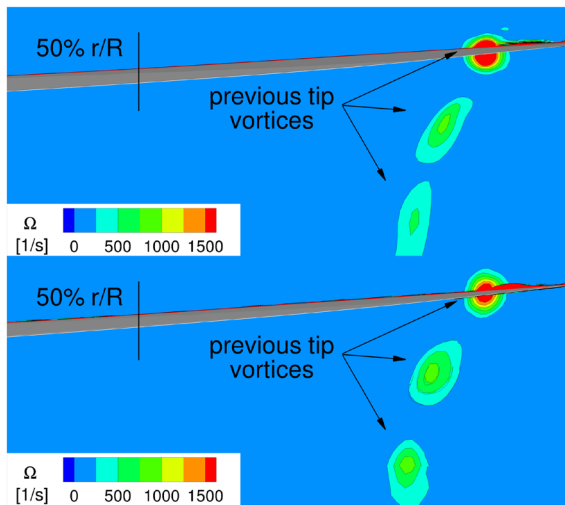


Fig. 42 Vorticity plots. Sliced through the low-fidelity optimized blade by ONERA, viewed from behind the rotor. Top: DLR's mono-coque mesh, bottom: DLR's Chimera setup, Kok $k-\omega$ turbulence model, fully turbulent

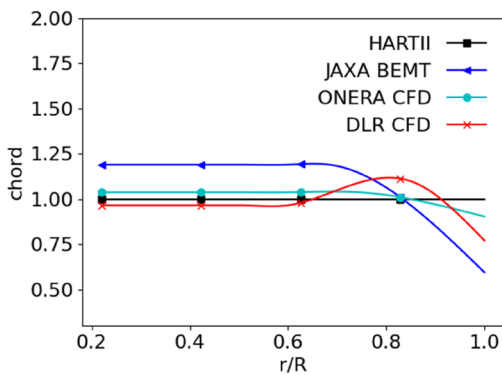


Fig. 43 Chord distribution of the CFD optimized blades

These studies conclude that the grid and solution process have a greater impact than the turbulence models or blade elasticity. Around $c_T/\sigma=0.1$, the first signs of stall can occur. At this point, the previous tip vortex may trigger stall and it is a matter of not only the employed spatial order, but also of the grid setup. In Fig. 42, the vorticity in the plane of the rotor is shown for DLR's mono-coque and the Chimera setup using the same numerical settings. The vortex strength is coincidentally almost the same for both grids, but the slightly skewed cells of the mono-coque mesh alter the oncoming vortex shape minimally. This, in combination with a slightly reduced blade flap, delays the stall at this point. The flap reduction, however, is also attributed to the grid. The round form of the second and third tip vortex gets successively lost with the mono-coque grid, while the cylindrical background mesh featuring

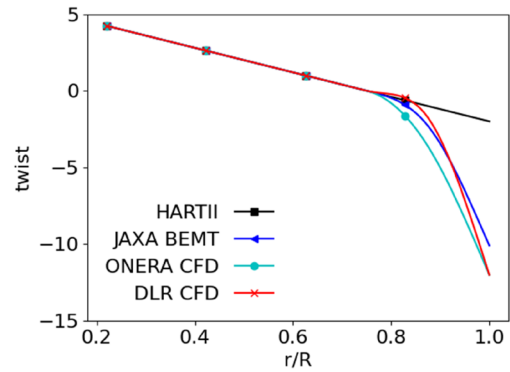


Fig. 44 Twist distribution of the CFD optimized blades

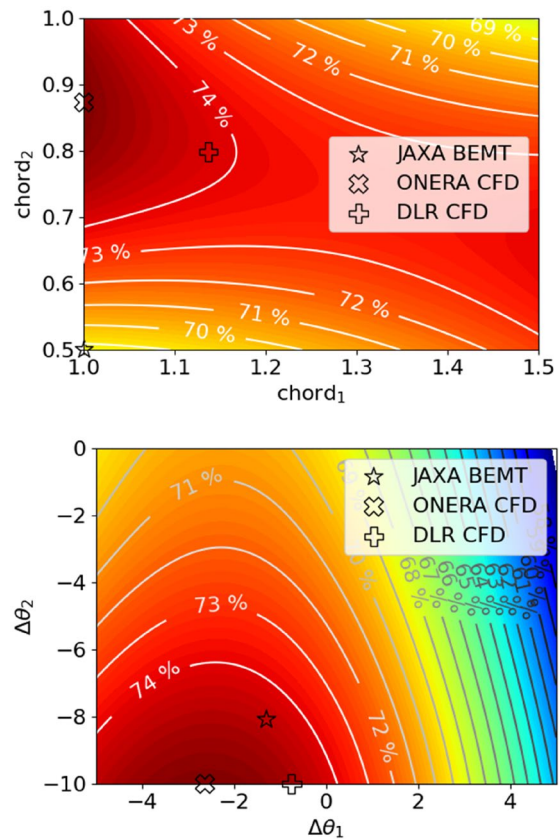


Fig. 45 Figure of Merit contour plots of ONERA's surrogate model sliced through the best sampled rotor of ONERA. Top: chord-plane, bottom twist-plane

more evenly distributed cells, the shape of these vortices is better preserved.

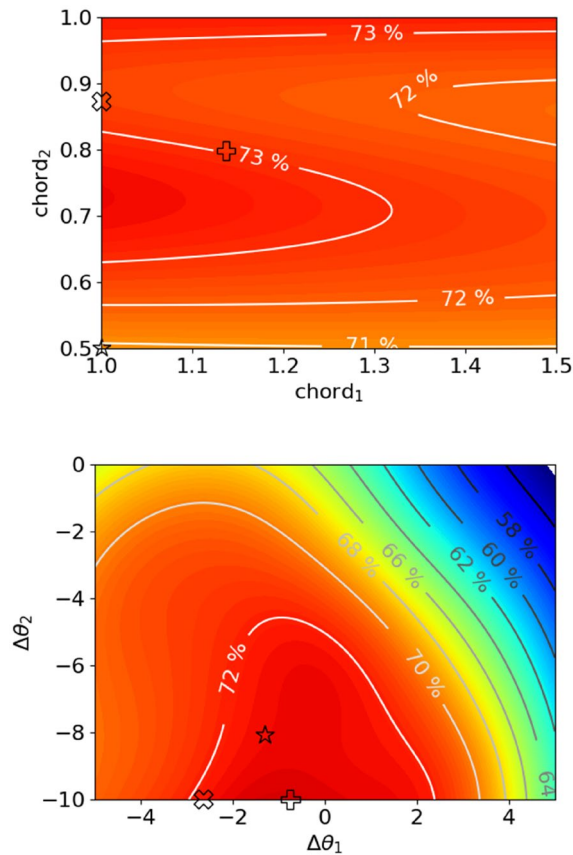


Fig. 46 Figure of Merit contour plots of the DLR's surrogate model sliced through the best sampled rotor of DLR. Top: chord-plane, bottom twist-plane

7 High-fidelity optimized blades

The chord and twist distributions of the CFD-based optimizations are sketched in Figs. 43 and 44, respectively. JAXA did not performed a high-fidelity optimization, thus their low-fidelity blade is compared side by side with the CFD blades in this section. However, a previous study by JAXA [1] has shown a high correlation between BEMT-based and CFD-based optimization results, and it is expected that the blade geometry would not change significantly.

Similar trends are observed for chord and twist distributions obtained from low- and high-fidelity optimizations, meaning a chord reduction and twist increase at the blade tip starting at $r/R = 0.8$. However, the high-fidelity optimizations provide a smaller chord reduction and a higher twist at the tip compared to the low-fidelity optimized blades, as the high-fidelity blades try to avoid the stall phenomenon.

To investigate the different outcomes of the chord distribution between ONERA and DLR, Figs. 45 and 46 depict the parameter sensitivities of ONERA and DLR with respect

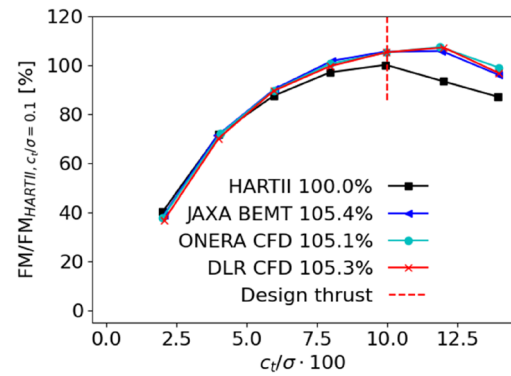


Fig. 47 Figure of Merit polars for all CFD optimized blades computed by JAXA's CFD approach

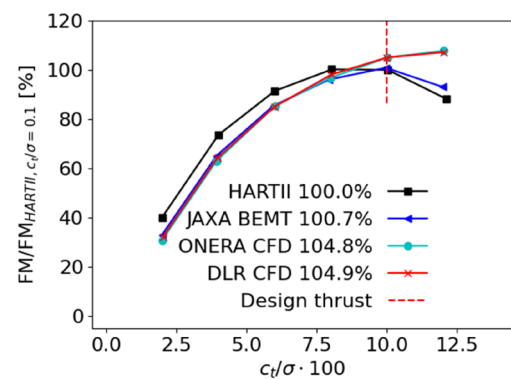


Fig. 48 Figure of Merit polars for all CFD optimized blades computed by ONERA's CFD approach

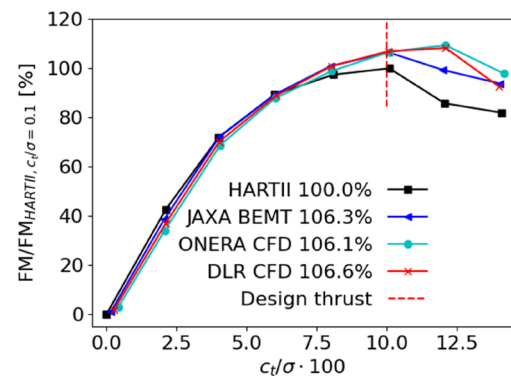


Fig. 49 Figure of Merit polars for all CFD optimized blades computed by DLR's CFD approach (SA-R LT)

to the chord and twist parameters seen from their respective optimum. These plots have been generated using the surrogate models from the optimization and may not capture the exact values that are further away from the optimum, but should nevertheless reflect the functional trend of these

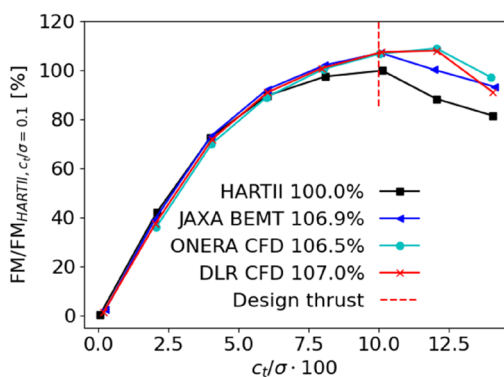


Fig. 50 Figure of Merit polars for all CFD optimized blades computed by DLR's CFD approach (SST FT)

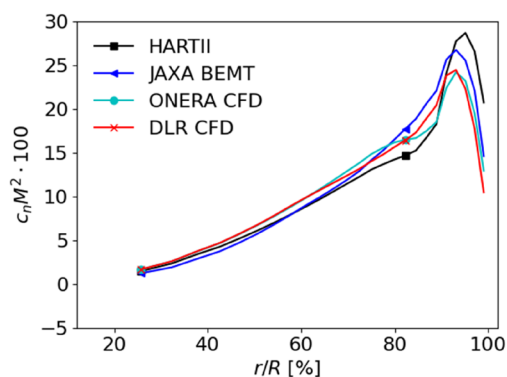


Fig. 52 Normal load distribution of all CFD optimized blades with ONERA's CFD approach at design thrust

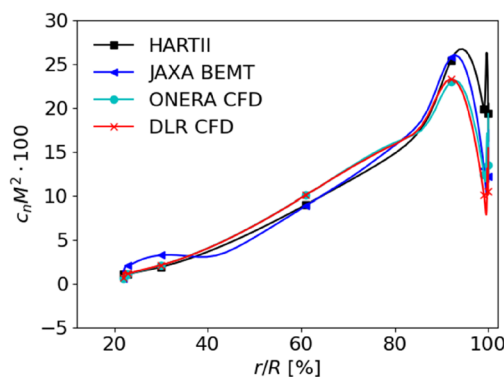


Fig. 51 Normal load distribution of all CFD optimized blades with JAXA's CFD approach at design thrust

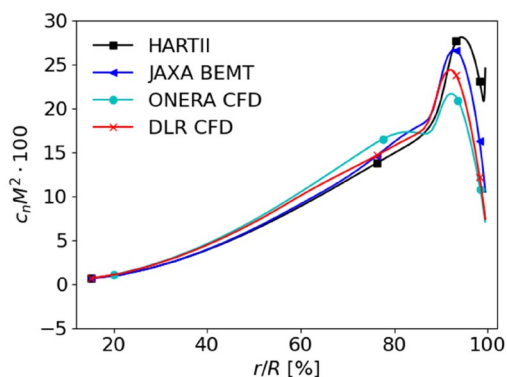


Fig. 53 Normal load distribution of all CFD optimized blades with DLR's (SA-R LT) CFD approach at design thrust

parameters sufficiently well. From a broad perspective, the functional behavior of both parameter groups is captured similarly by both partners. The agreement is better for the twist parameters, which also coincides with the findings from the previous JAXA-ONERA cooperation [3]. The two chord plots of ONERA and DLR show roughly the same region of improvement, yet the sensitivity of the chord parameters seems to be lower for DLR than for ONERA. Looking at the location of DLR's optimum in both plots, it seems that a further reduction in chord₁ may have been beneficial. Yet, the optimizer struggled with that due to the rather flat landscape of the DLR contour plot in contrast to the ONERA contour plot with steeper gradients.

In Figs. 47, 48, 49 and 50, the cross-examined Figure of Merit polars of these blades are shown. Looking at JAXA's results, the BEMT optimized blade proves to be more accurate than the CFD optimized blades, which is surprising at first. ONERA's results show a different picture, the two CFD optimized blades improve noticeably at the design thrust and beyond compared to the reference blade. In contrast to the other partners' results, the optimized blades show a reduced

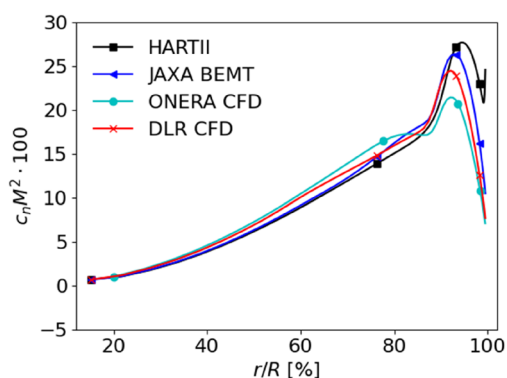


Fig. 54 Normal load distribution of all CFD optimized blades with DLR's CFD (SST FT) approach at design thrust

performance at thrusts below the design thrust. The DLR results show yet another tendency: regardless of the turbulence model setup, the DLR blade scores best, followed by JAXA's low fidelity blade and worst ranking is ONERA's CFD optimized blade, when looking at the design thrust.

However, at higher thrust, the CFD optimized blades prevail over the low fidelity optimized blades, as observed by ONERA as well.

In order to obtain a deeper understanding of the optimized blades, the normal load distributions computed by each partner for each blade are displayed in Figs. 51, 52, 53 and 54. Again, there is little difference between the two different turbulence modelling approaches for the DLR results. Compared to the ONERA results, the normal load distributions of the HART-II, JAXA BEMT and DLR CFD blades show a similar peak value, yet the ONERA blade has a lower peak with the DLR setups. Opposing this, JAXA's results feature slightly more triangular loads, mostly attributed to a reduced vortex strength in the simulation. Here, the trend of the peaks aligns well with ONERA, as the peaks of the ONERA and DLR blades are of similar magnitude for the ONERA and JAXA simulations. Overall, the ranking of the peaks is the same for all partners, demonstrating that the universal effects of the lift generation are well captured by all partners.

A certain commonality of the results is observed, as all JAXA and DLR optimized blades improve by 5–7% compared to the reference blade. Except for JAXA's low fidelity blade, this is also true for the ONERA results. Contrasting this with the previous lessons learned, a few contradictions can be resolved:

- JAXA has generally seen less severe, vortex induced separation effects due to a coarser background grid. This explains why the JAXA low fidelity optimized blade remains in good standing when cross-examined by JAXA with the other CFD optimized blades, even at higher thrusts. This also explains their previously found good correlation with the low-fidelity tools.
- The ONERA simulation has been more prone to induce (severe) separation, which explains the little gain of the JAXA low fidelity blade opposite the reference rotor.
- The DLR grid having slightly skewed cells delays the separation a little bit, but first signs are already visible for the HART-II and JAXA's low-fidelity optimized blade at design thrust. For higher thrusts, this separation becomes stronger, and therefore the JAXA blade performs worse than the other two CFD optimized blades at higher thrusts.

These results make it clear that, with the application of a more accurate method, a more reliable design can be generated.

8 Conclusion and outlook

This paper concludes work package/phase I of the JAXA-ONERA-DLR cooperation on rotor optimization. The task was to optimize the HART-II blade for hovering flight through current state-of-the-art methodologies by each research organization and to compare the findings to harmonize tools and approaches. It was decided to utilize a rather simple parameterization, which included two parameters for the chord length, one for the radial location of the inner chord length and two parameters for the twist distributions.

It was observed that for the baseline rotor, the low- as well as high-fidelity CFD simulations align well among the partners. When re-evaluating the low-fidelity optimized blades from each partner with CFD-based methods, discrepancies occur, resulting in a deeper investigation of the modelling approaches. The conclusions from these side-studies are as followed:

- The effect of turbulence modelling is roughly of the same order as including elasticity in the simulations here and relatively small compared to the effect of the grid employed.
- The effect of including the laminar-turbulent transition prediction is roughly of a similar magnitude as switching between SA-R, Kok $k-\omega$, Wilcox $k-\omega$ and Menter SST. The differences of the turbulence models were greater with the DLR grid using less grid points than they were with ONERA's grid featuring more grid points.
- The reason for elasticity playing a minor role in the presented optimizations is an unchanged quarter chord axis with respect to the baseline rotor, therefore no additional levers have been introduced from anhedral or sweep. It is thusly advised to be careful not to generalize this fact.
- The conservation of the tip vortex has a great impact on the performance prediction. JAXA employed a relatively coarse background grid and therefore resolved the weakest vortices, while the skewed cells of the periodic monocoque mesh without a background grid by DLR modified the vortex shape to a greater extent than the cylindrical background mesh by ONERA. Both effects lead to a delayed vortex induced stall phenomenon.
- Cross-checking ONERA's grid with DLR tools revealed very similar results between the partners. Upon building their own Chimera setups, DLR was able to find similar trends as ONERA.

Due to these studies, the outcome of the various results could be explained. Moving on to the high-fidelity optimization, the chance of separation for these blades has been greatly reduced and, thus, all partners found similar improvements for the high-fidelity optimized blades. From

the surrogate models of the high-fidelity optimizations, it was also discovered that altering the blade twist has a larger impact on the rotor performance than changing the chord distribution.

A few guidelines arising from the performed investigations are hereby postulated for the design and optimization of helicopter rotor blades in hover:

- Low-fidelity tools based on the blade element momentum theory (BEMT) or finite state models should be applied cautiously. They do not include a tip vortex model and thus lead to false load predictions. The resulting designs, however, may still be useful if cross-validated carefully with high-fidelity CFD.
- Performing efficient CFD simulations is a challenging task. While including many grid points, elasticity, laminar-turbulent transition prediction is logically a straightforward way to improve the simulation fidelity, it does not infer on what can be skipped to arrive at faster turnaround times.
 - With respect to the grid points, it was found that they need to be distributed correctly. The overset/Chimera interpolation requires similar cell sizes, while also the background grid also requires a certain resolution to capture at least the first tip vortex passage.
 - A monocoque periodic mesh will inherently have non-Cartesian cells. The cell skewness leads to distorted vortices. While highly efficient, these setups should be handled with care when employed near the maximum Figure of Merit, because the outboard separation is triggered by the tip vortices of the previous blades.
- Elasticity may be initially excluded, if the quarter chord axis of the rotor remains untouched, airfoils are not changed and the simulation can be sped up by this.
- Laminar-transition prediction has an impact on the absolute performance values as seen by the inexpensive empirical methods employed by DLR. However, if the cost for its inclusion is too high or laminar-transition prediction is not easily available, it may be neglected, as it seems to have a secondary impact on the final rotor designs.

As seen from these studies, different tools and approaches may lead to different designs. Thus, it should be ensured that the optimum retrieved still operates well under slightly altered conditions and with changing parameters, the cue being design robustness.

Overall, the first phase delivered many insights for all partners, highlighting the importance of such a cooperation. Without the comparison of others, the search for

improvements becomes even more difficult, and mistakes may remain undetected.

As an outlook, it is planned to investigate the HART-II rotor at a high advance ratio and reduced thrust requirements as required for compound helicopters. The research will be solely dedicated to this new flight condition to retrieve the single best design. In a later phase, it is planned to optimize the HART-II rotor for various flight conditions to obtain the aforementioned design robustness. The gathered knowledge will be applied to further improve the respective simulations.

Acknowledgements This paper is an extension of the work that was previously presented at 47th European Rotorcraft Forum, Virtual, United Kingdom, 7-10 September, 2021. We would also like to thank Beatrice Carter for proof-reading this paper.

Funding Open Access funding enabled and organized by Projekt DEAL.

Open Access This article is licensed under a Creative Commons Attribution 4.0 International License, which permits use, sharing, adaptation, distribution and reproduction in any medium or format, as long as you give appropriate credit to the original author(s) and the source, provide a link to the Creative Commons licence, and indicate if changes were made. The images or other third party material in this article are included in the article's Creative Commons licence, unless indicated otherwise in a credit line to the material. If material is not included in the article's Creative Commons licence and your intended use is not permitted by statutory regulation or exceeds the permitted use, you will need to obtain permission directly from the copyright holder. To view a copy of this licence, visit <http://creativecommons.org/licenses/by/4.0/>.

References

1. Sugiura, M., Tanabe, Y., Sugawara, H., Takekawa, K.: Optimal design of rotor blade for a winged compound helicopter at high advance ratio. In: Proceedings of the 76th Annual Forum, Virtual (2020).
2. Wilke, G., Länger-Möller, A., Tanabe, Y., Yasutada, Y., Sugiura, M., Sugawara, H.: Tackling the HARTII test case: a joint effort by DLR and JAXA. In: 6th Asian/Australian Rotorcraft Forum/Heli Japan 2017 (2017).
3. Sugiura, M., Tanabe, Y., Aoyama, T., Ortun, B., Bailly, J.: An ONERA/JAXA co-operative research on the assessment of aerodynamic methods for the optimization of helicopter rotor blades, phase II. In: 42nd European Rotorcraft Forum (2016).
4. Spletstößer, W. R., van der Wall, B. G., Junker, B., Schultz, K.-J., Beaumier, P., Delrieux, Y., Leconte, P., Crozier, P.: The ERATO Programme: wind tunnel results and proof of design for an aeroacoustically optimized rotor. In: 25th European Rotorcraft Forum (1999).
5. Wentrup, M., Yin, J., Kunze, P., Streit, T., Wendisch, J.-H., Schwarz, T., Pinacho, J.-P., Kicker, K., Fukari, R.: An overview of DLR compound rotorcraft aerodynamics and aeroacoustics activities within the CleanSky2 NACOR Project. In: AHS Forum (2018).
6. Fabiano, E., Mavriplis, D.: Adjoint-based aeroacoustic design-optimization of flexible rotors in forward flight. *J. Am. Helicopter Soc* **62–4**, 1–17 (2017)

7. Wang, L., Diskin, B., Biedron, R.T., Nielsen, E.J., Bauchau, O.A.: Evaluation of high-fidelity multidisciplinary sensitivity-analysis framework for multipoint rotorcraft optimization. *J. Aircr.* **57**, 830–842 (2020)
8. Fitzgibbon, T.A.: Advanced rotor blade design based on high-fidelity computational fluid dynamics (2021).
9. Wilke, G.: Variable-fidelity methodology for the aerodynamic optimization of helicopter rotors. *AIAA J.* **57**, 3145–3158 (2019)
10. van der Wall, B.G.: A comprehensive rotary-wing data base for code validation: the HART II International Workshop. *Aeronaut. J.* **115**, 91–102 (2011)
11. Kimura, K., Sugiura, M., Tanabe, Y., Wilke, G., Bailly, J.: Cooperative research on rotor blade optimization between JAXA-ONERA-DLR: results of phase I. In: *Fluid Mechanics Lecture/Aerospace Numerical Simulation Technology Symposium* (2020).
12. Peters, D.A., Boyd, D.D., He, C.J.: Finite-state induced-flow model for rotors in hover and forward flight. In: *43rd Annual Forum of the American Helicopter Society* (1987).
13. Basset, P.-M., Heuze, O., Prasad, J. V. R., Hamers, M.: Finite state rotor induced flow model for interferences and ground effect. In: *57th Annual Forum of the American Helicopters Society* (2001).
14. Benoit, B., Dequin, A.-M., Kampa, K., von Grünhagen, W., Basset, P.-M., Gimonet, B.: HOST, a general helicopter simulation tool for Germany and France. In: *56th Annual Forum of the American Helicopters Society*, Virginia (2000).
15. Bailly, J., Ortun, B., Delrieux, Y., de Rochettes, Y.M.: Recent advances in rotor aerodynamic optimization, including structural data update. *J. Am. Helicopter Soc* **62**, 1–11 (2017)
16. Wilke, G.: Quieter and greener rotorcraft: concurrent aerodynamic and acoustic optimization. *CEAS Aeronaut. J.* **12**, 495–508 (2021)
17. Tanabe, Y., Saito, S., Sugawara, H., Validation of high resolution CFD analysis for flowfield around a rotor. In: *The 40th JSASS Annual Meeting* (2009).
18. Cambier, L., Heib, S., Plot, S.: The Onera elsA CFD software: input from research and feedback from industry. *Mech. Ind.* **14**, 159–174 (2013)
19. Raddatz, J., Fassbender, J.K.: Block structured Navier–Stokes solver FLOWer. In: *MEGAFLOW—numerical flow simulation for aircraft design*. Berlin (2005).
20. Yamamoto, S., Daiguji, H.: Higher-order-accurate upwind schemes for solving the compressible Euler and Navier–Stokes equations. *Comput. Fluids* **22**(2–3), 259–270 (1993)
21. Shima, E., Kitamura, K.: On AUSM-family scheme for all speeds with shock detection for Caruncle-Fix. In: *Proceedings of 19th AIAA Computational Fluid Dynamics*, AIAA paper 2009–3544, June 2009, (2009).
22. Jameson, A., Schmidt, W., Turkel, E.: Numerical solution of the euler equations by finite volume methods using Runge–Kutta time-stepping schemes. In: *14th AIAA Fluid and Plasma Dynamics Conference* (1981).
23. Wilke, G.: New results in numerical and experimental fluid mechanics," 1 edn., vol. XIII, p. 790. Springer International Publishing (2022) (Accepted for publication).
24. Kitamura, K., Shima, E.: Towards shock-stable and accurate hypersonic heating computations: a new pressure flux for AUSM-family schemes. *J. Comput. Phys.* **245**, 62–83 (2013)
25. Yoon, S., Jameson, A.: Lower-upper symmetric-Gauss–Seidel method for the Euler and Navier–Stokes equations. *AIAA J.* **26**, 1025–1026 (1988)
26. Jameson, A., Baker, T. J.: Solution of the Euler equations for complex configuration. In: *Proceedings of 6th Computational Fluid Dynamics Conference Danvers*, AIAA paper 1983–1929, July 1983 (1983).
27. Radespiel, R., Rossow, C., Swanson, R.C.: Efficient cell-vertex multigrid scheme for the three-dimensional Navier–Stokes equations. *AIAA J.* **28**, 1464–1472 (1990)
28. Allmaras, S., Johnson, F. T., Spalart, P.: Modifications and clarifications for the implementation of the Spalart–Allmaras turbulence model. In: *Seventh International Conference on Computational Fluid Dynamics (ICCFD7)*, Big (2012).
29. Dacles-Mariani, J., Kwak, D., Zilliac, G.: On numerical errors and turbulence modeling in tip vortex flow prediction. *Int. J. Numer. Methods Fluids* **30**, 65–82 (1999)
30. Kok, J.C.: Resolving the dependence on freestream values for the k-turbulence model. *AIAA J.* **38**, 1292–1295 (2000)
31. Heister, C.C.: A method for approximate prediction of laminar-turbulent transition on helicopter rotors. *J. Am. Helicopter Soc.* **63**, 1–14 (2018)
32. Menter, F.R., Kuntz, M., Langtry, R.: Ten years of industrial experience with the SST turbulence model. *Heat Mass Transf.* **4**, 625–633 (2003)
33. Yeo, H., Potsdam, M., Ormiston, R.: Application of CFD/CSD to rotor aeroelastic stability in forward flight. In: *66th Annual Forum of the American Helicopters Society* (2010).
34. cadence, "The Choice for CFD Meshing," [Online]. <http://www.pointwise.com/>. Accessed 7 July 2021.
35. Maruyama, D., Bailly, D., Carrier, G.: High-quality mesh deformation using quaternions for orthogonality preservation. *AIAA J.* **52**, 2712–2729 (2014)
36. Benoit, C., Péron, S., Landier, S.: Cassiopee: a CFD pre- and post-processing tool. *Aerosp. Sci. Technol.* **45**, 272–283 (2015)
37. Allen, C.B.: CHIMERA volume grid generation within the EROS code. *Proc Inst Mech Eng Part G J Aerosp Eng* **214**, 125–140 (2000)
38. Jones, D.R., Schonlau, M., Welch, W.J.: Efficient global optimization of expensive black-box functions. *J. Glob. Optim.* **13**, 455–492 (1998)
39. Kanazaki, M., Jeong, S., Yamamoto, K.: High-lift system optimization based on the Kriging model using a high-fidelity flow solver. *Trans. Jpn. Soc. Aeronaut. Space Sci.* **49**, 169–174 (2006)
40. Kanazaki, M., Yokokawa, Y., Murayama, M., Ito, T., Jeong, S., Yamamoto, K.: Nacelle chine installation based on wind-tunnel test using efficient global optimization. *Trans Jpn Soc Aeronaut Space Sci* **51**, 146–150 (2008)
41. Bailly, J., Bailly, D.: Multifidelity aerodynamic optimization of a helicopter rotor blade. *AIAA J.* **57**, 3132–3144 (2019)
42. Kennedy, M.C., O'Hagan, A.: Predicting the output from a complex computer code when fast approximations are available. *Biometrika* **87**, 1–13 (2000)
43. Han, Z.-H., Görtz, S.: A hierarchical kriging model for variable-fidelity surrogate modeling. *AIAA J.* **50–9**, 1885–1896 (2012)
44. Takeda, S., Sugiura, M., Tanabe, Y., Sugawara, H., Kanazaki, M., Harigae, M.: Influence of pre-twist distribution at the rotor blade tip on performance during hovering flight. *Trans. Jpn. Soc. Aeronaut. Space Sci.* **58**, 39–44 (2015)
45. Sugiura, M., Tanabe, Y., Sugawara, H., Kanazaki, M.: Computationally efficient and high fidelity optimization of rotor blade geometry. In: *40th European Rotorcraft Forum* (2014).
46. Storn, R., Price, K.: Differential evolution—a simple and efficient adaptive scheme for global optimization over continuous spaces. *J. Glob. Optim.* **11**, 341–359 (1997)
47. Nelder, J.A., Mead, R.: A simplex function for minimization. *Comp. J.* **8–1**, 308–313 (1965)
48. Küfmann, P., Bartels, R., van der Wall, B. G., Schneider, O., Holthusen, H., Gomes, J., Postma, J.: The first wind tunnel test of the DLR's multiple swashplate system: test procedure and preliminary results. In: *AHS 72nd Annual Forum* (2016).
49. Imiela, M.: High-fidelity optimization framework for helicopter rotors. *Aerosp. Sci. Technol.* **23**, 2–16 (2012)

50. Imiela, M.: Mehrpunktoptimierung eines Hubschrauberrotors im Schweben- und Vorwärtsflug unter Berücksichtigung der Fluid-Struktur-Wechselwirkung (2012).
51. Stanger, C., Hollands, M., Kessler, M., Krämer, E.: Adaptation of the dynamic rotor blade modelling in CAMRAD for fluid-structure coupling within a blade design process. In: 18. DGLR-Fach-Symposium der STAB (2012).
52. Desvigne, D., Coisson, R., Michel, B. R., Thomas, A., Pinacho, J. P., Roca León, E.: Multi-objective industrial optimization of

high-speed helicopter main rotor blades with dynamically-adapted structural properties. In: 45th European Rotorcraft Forum (2019).

Publisher's Note Springer Nature remains neutral with regard to jurisdictional claims in published maps and institutional affiliations.